Nano Research

ISSN 1998-0124 CN 11-5974/O4
https://doi.org/10.26599/NR.2026.94908502

Research Article

Enhanced hydrogen storage kinetics of magnesium hydride enabled by graphene-supported Pd–Ni bimetallic nanocatalysts

Baozhou Zhao[1](✉), Yuan Li[2,3], Haiguang Gao[4], Jia Guo[1], Xiaohao Shi[1], Qingyun Shi[2,3], Xinxin Wang[2,3], Runkuo Han[2,3], Yufei Liu[2,3], Qingshuang Wang[5], Chaoyue Zhao[6], Jianguang Yuan[2,3](✉)

[1] School of Medical and Health Engineering,Changzhou University, Changzhou 213164, China

[2] State Key Laboratory of Rare Earth Resource Utilization, Changchun Institute of Applied Chemistry, Chinese Academy of Sciences, Changchun 130022, China

[3] School of Applied Chemistry and Engineering, University of Science and Technology of China (USTC), Hefei 230026, China

[4] Jiangsu Key Laboratory of Advanced Catalytic Materials and Technology, School of Petrochemical Engineering, Changzhou University, Changzhou 213164, China

[5] College of Life Science and Technology, Changchun University of Science and Technology, Changchun 130022, China

[6] Jilin JiEn Nickel Industry Co., Ltd., Jilin 132311, China

Nano Res., **Just Accepted Manuscript** • https://doi.org/10.26599/NR.2026.94908502

https://www.sciopen.com/journal/1998-0124 on Jan. 28, 2026

Just Accepted

TABLE OF CONTENTS (TOC)

Enhanced Hydrogen Storage Kinetics of Magnesium Hydride Enabled by Graphene-Supported Pd–Ni Bimetallic Nanocatalysts

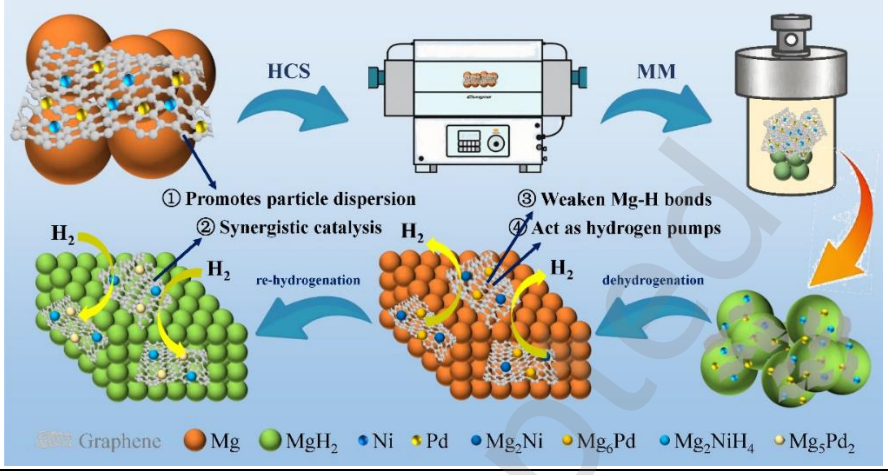

A novel Mg-PdNi@rGN composite is prepared by integrating graphene nanosheet–supported Pd-Ni bimetallic catalysts, which reduces the initial hydrogen release temperature, increases the hydrogen release rate, and improves the cycling performance of MgH_2, which can be attributed to the PdNi alloy inducing interface electron redistribution, effectively weakening the Mg-H bond.

Nano Research

Open Access

Research Article

Enhanced hydrogen storage kinetics of magnesium hydride enabled by graphene-supported Pd–Ni bimetallic nanocatalysts

Baozhou Zhao[1] ✉, Yuan Li[2,3], Haiguang Gao[4], Jia Guo[1], Xiaohao Shi[1], Qingyun Shi[2,3], Xinxin Wang[2,3], Runkuo Han[2,3], Yufei Liu[2,3], Qingshuang Wang[5], Chaoyue Zhao[6], and Jianguang Yuan[2,3] ✉

[1] *School of Medical and Health Engineering,Changzhou University, Changzhou 213164, China*
[2] *State Key Laboratory of Rare Earth Resource Utilization, Changchun Institute of Applied Chemistry, Chinese Academy of Sciences, Changchun 130022, China*
[3] *School of Applied Chemistry and Engineering, University of Science and Technology of China (USTC), Hefei 230026, China*
[4] *Jiangsu Key Laboratory of Advanced Catalytic Materials and Technology, School of Petrochemical Engineering, Changzhou University, Changzhou 213164, China*
[5] *College of Life Science and Technology, Changchun University of Science and Technology, Changchun 130022, China*
[6] *Jilin JiEn Nickel Industry Co., Ltd., Jilin 132311, China*

Received: 7 January 2026; **Revised:** 26 January 2026; **Accepted:** 28 January 2026

✉Address correspondence to Jianguang Yuan, jgyuan@ciac.ac.cn; Baozhou Zhao, zbzzsj@cczu.edu.cn

Cite this article: *Nano Research*, **2026**, *19*, 94908502. https://doi.org/10.26599/NR.2026.94908502

ABSTRACT: To address the sluggish hydrogen sorption kinetics of MgH_2, a novel Mg-PdNi@rGN composite is prepared by integrating graphene nanosheet–supported Pd-Ni bimetallic catalysts via a combined hydriding combustion synthesis (HCS) and mechanical milling (MM) strategy. The composite exhibits exceptional hydrogen storage performance, with a dehydriding onset temperature of ~140 °C and a peak desorption of 256.9 °C (94.7 °C lower than pure Mg), and an activation energy of only 70.5 kJ mol^{-1}. Remarkably, the composite achieves 6.46 wt% hydrogen uptake within 100 s at 100 °C and releases 6.70 wt% H_2 in 400 s at 300 °C, maintaining 98.95% capacity retention after 15 cycles. First-principles calculations elucidate that the PdNi nanocatslyst induces interfacial electron redistribution, effectively weakening Mg-H bonding. Complementary experimental characterizations reveal that the in-situ formed Mg_2NiH_4 and MgPd phases serve as efficient hydrogen transport channels, while the graphene matrix simultaneously enhances thermal/electrical conductivity and suppresses particle agglomeration. This work establishes a new paradigm for the rational design of high-performance Mg-based hydrogen storage materials through the synergistic coupling of bimetallic catalysts with two-dimensional carbon supports.

KEYWORDS: hydrogen storage, MgH_2, PdNi@rGN, synergistic integration

1 Introduction

To achieve the goal of "peak carbon emissions and carbon neutrality", clean energy is flourishing [1–6]. Various types of power equipment are being widely researched and promoted for application [7–11]. Fuel cell devices and vehicles based on hydrogen energy require an efficient and safe hydrogen storage medium, which has not yet been successfully realized to date[12–15]. Magnesium hydride (MgH_2) is a potential practical medium for hydrogen storage materials owing to its high hydrogen capacity, natural abundance, recyclability, environmental benignity, and low cost [16–20]. However, the high desorption temperatures (at least 573 K) and slow kinetics limit its practical application. To overcome these intrinsic drawbacks, numerous strategies, including nanostructuring, catalytic doping, and alloying have been extensively explored [21–28]. Despite these efforts, developing Mg-based materials that simultaneously exhibit rapid hydrogen sorption kinetics and moderate operating temperatures remains a formidable challenge. Therefore, designing new MgH_2-based composites with optimized catalytic interfaces and microstructures is of great significance for achieving practical on-board hydrogen storage.

Recent studies have demonstrated that incorporating transition metal catalysts such as, nickel (Ni), cobalt (Co), palladium (Pd), and copper (Cu), titanium (Ti), niobium (Nb), and vanadium (V), has manifested improved kinetics and a decrease in activation energies [29–36]. In particular, Pd and Ni have shown remarkable catalytic activity in promoting hydrogen absorption and desorption processes [37,38]. Nevertheless, these reactions typically require elevated operating temperatures, where severe particle growth and agglomeration can occur, leading to a gradual deterioration of kinetic performance [39–41]. To mitigate this issue, direct particle-particle contact must be minimized. Immobilizing catalytic nanoparticles onto porous or high-surface area supports has proven to be an effective strategy for restricting particle coalescence and maintaining catalytic activity [42-44]. The porous supports framework not only prevents sintering but also ensures uniform particle dispersion and facilitates hydrogen diffusion. In this work, graphene nanosheets are employed as an advanced support matrix to inhibit particle growth of transition metal catalysts

and to enhance both the structural stability and hydrogen transport properties of the composite system.

Graphene, a single- or few-layer carbon sheet with exceptional physical and chemical properties, has attracted tremendous attention in recent years owing to its ultrahigh specific surface area, superior electrical and thermal conductivity, and remarkable mechanical strength, graphene has found extensive applications in energy storage, catalysis, electronics, and sensing [45–49]. Moreover, carbon-based materials are known to facilitate the reversible de/hydrogenation of MgH_2 by improving charge transfer and providing efficient diffusion pathways [50–54]. Thus, graphene nanosheets (GN) derived from graphite exfoliation, are expected to exert a pronounced catalytic effect on MgH_2, further enhancing its hydrogen storage performance. The flexible, delaminated architecture and abundant interlayer space can effectively suppress hydride particle agglomeration, thereby promoting rapid and reversible hydrogen sorption [55–57]. As a result, it has been well established that transition metals, carbon materials, and metal-carbon composites have a favorable impact upon the hydrogen sorption/desorption kinetics of magnesium hydroxide. Liu et al [58]. discovered the MgH_2 composite with 5% Ni@rGO obtained by ball milling for 10 hours under 0.5 MPa H_2 pressure showed enhanced sorption kinetics and a lower sorption temperature in comparison to pure MgH_2, and the composite can desorb 6.0 wt% H_2 within 10 minutes at 573 K even after a total of nine cycles. A multi-component catalyst was synthesized by Jia et al [59] composed of active carbon (AC) and Ni-VO_x and discovered that the Mg-Ni-VO_x/AC composite has the potential to absorb 6.2 wt% hydrogen in less than one minute at 423 K under a 2 MPa hydrogen pressure and can potentially desorb 6.5 wt% hydrogen in less than ten minutes at 573 K.

Building upon the above advances and seeking to overcome the remaining challenges in Mg-based hydrogen storage, this work presents a novel strategy for achieving highly efficient catalytic enhancement. A graphene nanosheet-supported bimetallic Pd-Ni catalyst (designated as PdNi@GN by mass ratio) was incorporated into magnesium hydride through a synergistic hydriding combustion synthesis (HCS) and mechanical milling (MM) process. The PdNi@GN catalyst itself was uniquely synthesized via a two-step chemical reduction method to ensure uniform nanoparticle dispersion and intimate metal-graphene interaction. The underlying hypothesis is that the highly reactive Mg matrix derived from HCS+MM processing can effectively couple with the superior catalytic activity of the Pd-Ni nanocatslyst and the conductive graphene framework, resulting in exceptional hydrogen sorption performance. This study systematically investigates the influence of the PdNi@GN additive on the microstructure and hydrogen sorption properties (kinetics, capacity, and cycling stability) of the magnesium-based composites, elucidating the interfacial mechanisms governing their remarkable enhancement in hydrogen storage efficiency.

2 Results and discussion

A two-step chemical reduction technique was utilized for the first time for synthesizing PdNi@rGN nanoparticles. Specifically, Ni@rGN and Pd@rGN nanoparticles were synthesized by a high-temperature solid-phase reduction method and a wet-chemical reduction method, respectively. The crystal structures have been identified and refined using the X-ray powder diffraction (XRD). The XRD patterns of the oxidized rGN, the as-prepared Ni@rGN, and PdNi@rGN nanoparticles are shown in Figure 1a. The major sharp peak in the oxidized graphene nanoplates, centered at $2\theta \approx 26.4°$, can be attributed to characteristic amorphous carbon (JCPDS No. 04-0850) (Fig. 1(a)). The XRD pattern of the intermediate sample Ni@rGN (Figure 1a) shows obvious diffraction peaks of Ni (JCPDS No. 15-0806) attributed to the (111), (200), and (220) plane reflections. In contrast, the PdNi@rGN catalyst shows additional peaks associated with fcc Pd (JCPDS No. 04-0850), including the (111), (200), (220), and (311) planes, confirming the successful incorporation of Pd and Ni nanoparticles onto the rGN framework. The average crystallite sizes of Pd and Ni, estimated using the Scherrer equation (Eq. 1), are approximately 8.5 nm and 12.6 nm, respectively~~, indicating the formation of uniformly dispersed nanoscale alloy domains~~.

$$D_{hkl}=-K\lambda/\beta\cos\theta \quad \text{(Eq.1)}$$

Transmission electron microscopy (TEM) was employed to elucidate the morphology and dispersion of Pd and Ni nanoparticles on the graphene nanosheets. The PdNi@rGN nanoparticles (Fig. 1(b)) exhibit a spherical morphology with particle sizes ranging from 20 to 50 nm, uniformly anchored on the surface of graphene nanoplates. The individual Pd and Ni nanoparticles display diameters of approximately 5-20 nm, and no obvious agglomeration is observed, indicating excellent dispersion within the rGN matrix. Compared with Ni@rGN, the particle size in PdNi@rGN is markedly reduced, confirming that the two-step chemical reduction process effectively suppresses nanoparticle coalescence relative to high-temperature solid-state reduction. The selected area electron diffraction (SAED) patterns further demonstrate the presence of Pd, Ni, and C in Figure 1c, and agree with the XRD result. It exhibits a distinct ring-like structure and diffraction spots, with the spots corresponding to the plane reflections of C (100), Ni (200), and Pd (300). (220). The high-resolution transmission electron microscopy (HRTEM) images (Figs. 1(d)-1(f)) reveal lattice fringes with interplanar spacings of 0.2237 nm, corresponding to the (111) crystallographic planes of Pd, and 0.2025 nm, matching the (111) planes of Ni. Additionally, lattice fringes with a spacing of 0.3307 nm are attributed to the graphene (GN) lattice structure. Elemental mapping by energy-dispersive X-ray spectroscopy (EDS, Figs. 1(g)-1(k)) clearly confirms the homogeneous spatial distribution of Pd, Ni, and C throughout the composite. These observations demonstrate the successful formation of uniformly dispersed Pd–Ni nanoparticles intimately anchored on the conductive graphene support, a structural configuration expected to provide abundant active interfaces and facilitate efficient electron and hydrogen transport in subsequent storage reactions.

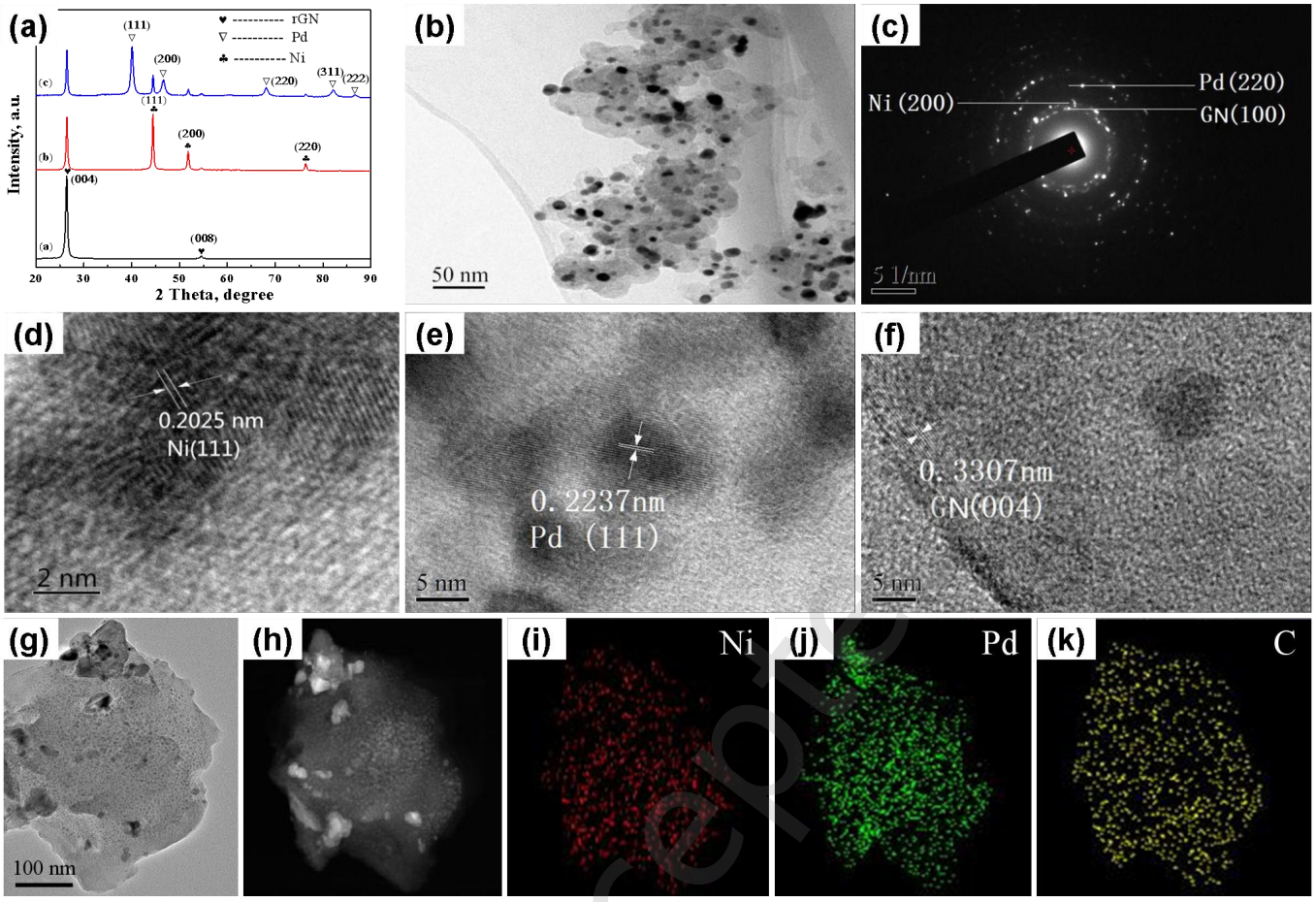

Figure 1 XRD pattern (a) ; TEM images (b-h); corresponding EDS mapping of the PdNi@rGN catalyst (i-k).

The XRD patterns of the HCS+MM-processed samples (Fig. S1(a) in the ESM) reveal that the diffraction peaks corresponding to MgH_2 and Mg are significantly broadened and weakened compared with those of the HCS-derived specimens, indicating substantial grain refinement and the accumulation of lattice strain during the milling process. Mechanical milling not only introduces numerous crystal defects and grain boundaries but also promotes the uniform distribution of in situ-formed Mg_2NiH_4 and MgPd phases, which are thermodynamically favorable for hydrogenation. The extent of peak broadening increases with higher MgH_2 content, suggesting that progressive hydride formation enhances milling efficiency by facilitating repeated fracturing and cold welding of particles. The average grain size of MgH_2 in Mg-PdNi@rGN, Mg-Ni@rGN, Mg-Pd@rGN, Mg-rGN, and Mg is predicted to be 18.5, 11.8, 9.6, and 8.7 nm, respectively, using Scherrer's equation (Fig. S1(b) in the ESM). The pronounced grain refinement and defect formation during high-energy milling markedly increase the active surface area and diffusion pathways, which are expected to enhance hydrogen absorption–desorption kinetics in the composite system. To validate the nanostructure in its as-milled state, transmission electron microscopy TEM was utilized to examine the composites for determining the presence and dispersion of various phases (Figs. S2(d)-S2(f) in the ESM). The PdNi@GN was broken down and dispersed uniformly on the MgH_2/Mg base during sorption and desorption. Pd, Ni, and C were all uniformly scattered on the surface of elemental Mg, providing more active catalytic sites and hydrogen diffusion channels and resulting in high catalytic efficiency (FigS. S1(c)-S1(g) in the ESM). More importantly, the presence of evenly distributed C acts as an effective heat exchanger during sorption and desorption, assisting in the thermal control of MgH_2. TEM images and related selected area electron diffraction (SAED) patterns of the hydrogenated Mg-PdNi@GN composite are shown in Figs. S2(a)-S2(c) in the ESM. The composite exhibits a typical aggregate structure in the bright field image, with the black particles scattered throughout the grey matrix. High-resolution TEM (Fig. S2(b) in the ESM) shows lattice fringes with interplanar spacings of 0.2185 nm, 0.2270 nm, and 0.3314 nm, corresponding to the (110) planes of MgPd, the (200) planes of MgH_2, and the (002) planes of graphene nanosheets, respectively. The SAED pattern (Fig. S2(c) in the ESM) exhibits well-defined concentric rings with discrete diffraction spots, confirming the presence of Ni (200), Pd (311), and C (002) planes and indicating a fine-grained polycrystalline structure. The SAED pattern demonstrates the presence of individual diffraction spots spread throughout each discernible ring, with the spots corresponding to the plane reflections of Ni (200), Pd (311), and C (002) from the inner to outer. The coexistence of Mg, MgH_2, MgPd, Mg_2NiH_4, and carbon within the framework is consistent with XRD observations. Additionally, the SAED pattern indicates that the synthesized sample contains a mixture of MgPd, Mg_2NiH_4, and C.

To gain a better understanding of the catalytic effects of Ni,

Pd, and GN on the hydrogen-storage characteristics of MgH_2, the hydriding curves of the HCS+MM samples Mg-PdNi@rGN, Mg-Ni@rGN, Mg-Pd@rGN, Mg-rGN, and Mg at temperatures of 100, 200, and 250 °C are clearly shown in Figs. 2(a)-2(c). As expected, decreasing the temperature from 250 to 100 °C leads to slower absorption kinetics.

Notably, Mg-PdNi@rGN exhibits outstanding hydrogen uptake at 100 °C, reaching a saturated capacity of 6.46 wt% within 100 s. Mg-Ni@rGN absorbs 6.00 wt% H_2 under identical conditions, whereas Mg-Pd@rGN, Mg-rGN, and Mg show negligible hydrogen uptake, indicating that Ni dominates low-temperature catalytic activity. At 200 °C and above, all composites except pristine Mg demonstrate rapid hydriding kinetics, with Mg-Pd@rGN surpassing Mg-Ni@rGN in hydrogen capacity, highlighting the temperature-dependent superiority of Pd in promoting hydrogenation. The enhanced hydrogenation of Mg during the HCS process, particularly in the presence of Pd, is reflected in the XRD patterns of the Mg-PdNi@rGN composites and is a key factor governing subsequent hydriding performance. Mg-PdNi@rGN achieves the highest hydrogen storage, with capacities of 6.87 wt% at 250 °C. Short-term absorption tests over 800 s further confirm its rapid kinetics. These results indicate that Ni predominantly accelerates hydrogen absorption at low temperatures, while Pd significantly enhances hydrogen capacity at elevated temperatures, and the combination with graphene ensures uniform nanoparticle dispersion and efficient hydrogen transport.

Thermal desorption curves were used to investigate the improved impacts of PdNi@GN on the dehydrogenation performance of MgH_2. Figure S3(a) in the ESM shows the hydrogen release profiles at various temperatures for the HCS+MM samples Mg-PdNi@rGN, Mg-Ni@rGN, Mg-Pd@rGN, Mg-rGN, and Mg. All composites exhibit significantly reduced desorption temperatures compared with pure MgH_2 due to the catalytic action of the doped additives Upon heating to 330 °C, pure MgH_2 releases ~4.45 wt% H_2, whereas Mg-rGN, Mg-Pd@rGN, Mg-Ni@rGN, and Mg-PdNi@rGN release 4.90, 6.20, 6.00, and 5.78 wt% H_2, respectively (Fig. S3(b) in the ESM). Mg-PdNi@rGN exhbits the fastest dehydriding kinetics, with a dehydriding initiation temperature of around 140 °C (at which hydrogen begins to release), which is 50 °C lower in comparison to that of Mg. These results indicate that the incorporation of Pd, Ni, and graphene serves as an effective catalytic system, promoting hydrogen desorption at lower temperatures and facilitating rapid dehydrogenation.

Hydrogen desorption of all samples is negligible at low temperatures due to the high thermodynamic stability of MgH_2. Figures 2(d)-2(f) depicts the dehydriding curves of the HCS+MM samples Mg-PdNi@rGN, Mg-Ni@rGN, Mg-Pd@rGN, Mg-rGN, and Mg at temperatures of 200, 250, and 300 °C. During desorption, the initial hydrogen pressure is 0.005 MPa. The hydrogen desorption curves for all samples at 200 °C are shown in Fig. 2(d). Although the amount of desorbed hydrogen is limited at such low temperatures, the evident disparity in the rate of hydrogen desorption rate among the Ni-, Pd-, rGN-, and composite specimens demonstrate the distinct catalytic properties of Ni, Pd, and graphene nanoplates. Ni@rGN enhances the dehydriding rate relative to the graphene-only sample, while Pd@rGN exhibits superior performance to rGN alone, indicating that graphene primarily serves as a dispersion and conductivity support. Surprisingly, however, the appropriate mix of transition metal Ni and Pd with graphene nanoplates has a significant effect on dehydriding behavior. In comparison to the other samples, the Mg-PdNi@rGN sample performs the best, desorbing approximately 6.73 wt% of hydrogen in the 1800s at a comparatively low temperature of 300 °C. Additionally, after 400 s at 300 °C, the hydrogen desorption capability of Mg-PdNi@rGN is raised to 6.70 wt%.

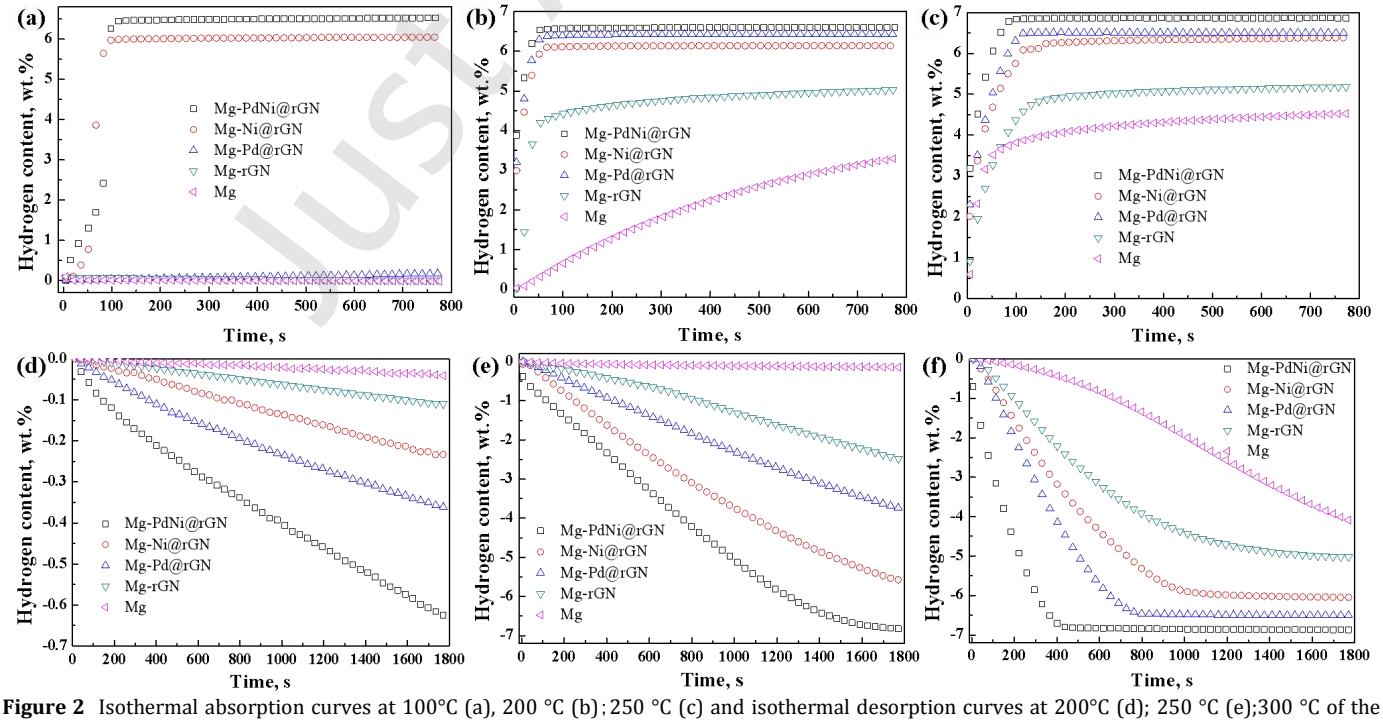

Figure 2 Isothermal absorption curves at 100°C (a), 200 °C (b)；250 °C (c) and isothermal desorption curves at 200°C (d); 250 °C (e);300 °C of the composites.

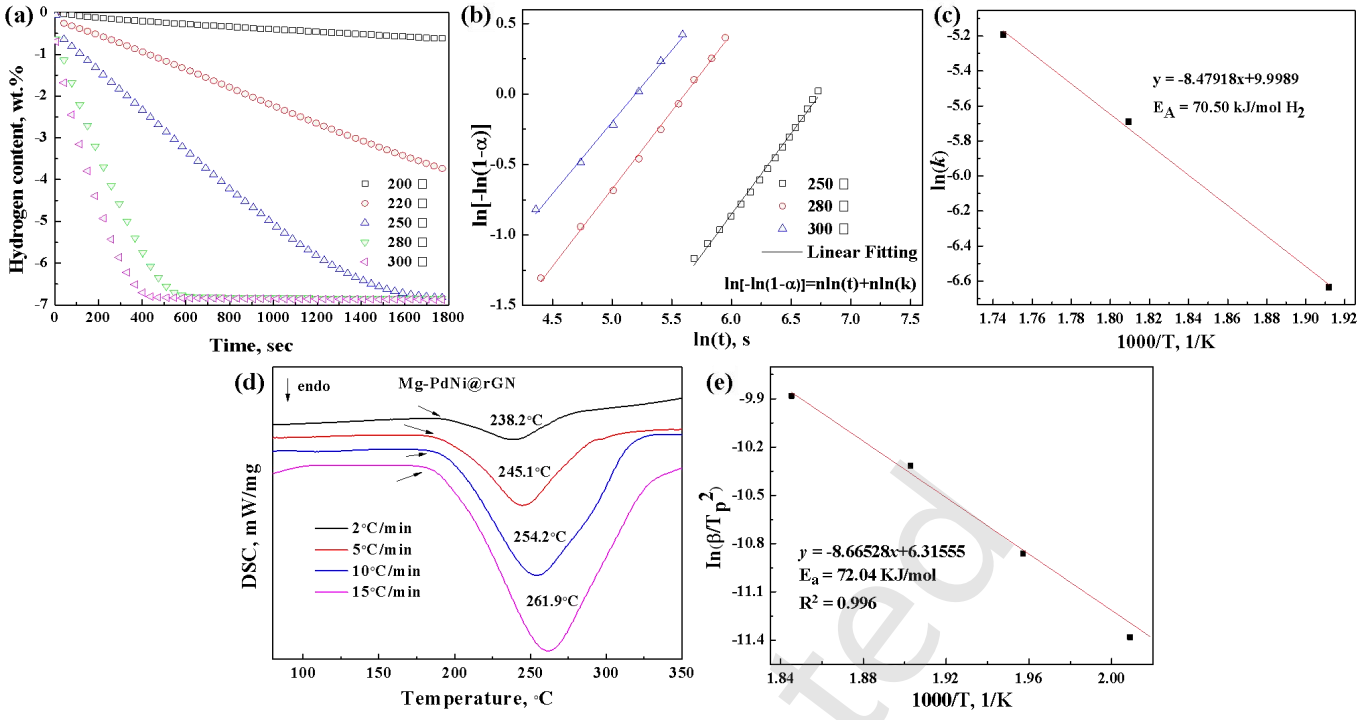

Figure 3 Arrhenius plots of the dehydriding kinetics of the Mg-PdNi@rGN composite(a-c);DSC curves and Kissinger's plots of Mg-PdNi@rGN at different heating rates of 2, 5, 10 and 15°C min^{-1} under Ar flow (d-e).

Given its exceptional hydriding and dehydriding behavior, Mg-PdNi@rGN was further investigated for activation energy (E_a), reaction enthalpy, thermal decomposition behavior, and cyclic stability. Isothermal hydrogen desorption experiments (Fig. 3(a)) show smooth desorption profiles, with ~3.74 wt% H_2 released within 30 min at 220 °C, underscoring the composite's outstanding low-temperature performance. To get an additional understanding of the hydrogen desorption behavior of the material, the activation energy (E_a) is measured. Geometrical contraction models (R2 and R3), the Johnson-Mehl-Avrami (JMA) model, diffusion models (D1, D2, D3, and D4), and zero-order chemisorption model are the most frequently employed models for the investigation of hydrogenation/dehydrogenation reactions taking place in solid-state. The JMA model provides the best fit to the desorption curves (correlation coefficient $R^2 > 0.99$), and is therefore employed to characterize the hydrogen release kinetics of the Mg-PdNi@rGN composite.

$$\ln[-\ln(1-\alpha)] = n\ln t + n\ln k \quad \text{(Eq.2)}$$

In the JMA model, the Avrami exponent n reflects the nucleation mechanism, growth dimensionality, and the rate-limiting process, while α denotes the fraction of hydrogen desorbed at time t, and k is the corresponding rate constant. The dependence of n on the growth dimensionality, rate-limiting process, and nucleation behavior have been elaborated in detail in ref [53]. The JMA plots of $\ln[-\ln(1-\alpha)]$ *vs* $\ln(t)$ for the desorption data of the Mg-PdNi@GN at various temperatures precisely 250, 280, and 300 °C have been illustrated in Fig. 6(b). Within the range of $0.1 < \alpha < 0.7$, the plots show a good linearity ($R^2 > 0.99$). For each temperature, the rate constant can be obtained by plotting a straight line representing $\ln[-\ln(1-\alpha)]$ *vs* $\ln(t)$, with the slope n and the intercept $n\ln(k)$.

The activation energy (E_a) for hydrogen desorption was determined using the Arrhenius equation:

$$E_A = -\mathrm{RT}\ln(k/k_0) \quad \text{(Eq.3)}$$

Where k_0 is the Arrhenius constant, k is the dehydrogenation kinetic rate constant, E_a is the activation energy. The Arrhenius plots for the dehydriding kinetics of the Mg-PdNi@rGN are shown in Fig. 3(c). The activation energy for hydrogen desorption from Mg-PdNi@rGN is estimated to be 70.5 kJ mol^{-1} H_2, which is substantially lower than that of commercial MgH_2 (153 kJ mol^{-1} H_2). This significant reduction confirms that the PdNi@rGN catalyst markedly enhances the dehydrogenation kinetics of MgH_2 by lowering the energy barrier for hydrogen release. Differential scanning calorimetry (DSC) was employed to investigate the thermal hydrogen desorption behavior of Mg-PdNi@rGN at various heating rates (Fig. 3(d)). As the ramping rate increased from 2 to 15 °C min^{-1}, the peak temperature grew monotonically. Mg-PdNi@rGN exhibits a single endothermic peak at 238, 245.1, 254.2, and 261.9 °C, corresponding to the breakdown of the main phase MgH_2 The onset temperature of dehydriding remained nearly constant between 160 and 180 °C across all ramp rates, indicating consistent catalytic activity of the HCS+MM-processed composite. Therefore, it is worthwhile to determine the activation energy involved in the desorption process by DSC measurements at various ramping rates, in an attempt to attain a better understanding of the reaction mechanism. The Kissinger method was also employed for the estimation of the activation energy.

$$\ln\left(\frac{\beta}{T_p^2}\right) = -\frac{E_a}{\mathrm{R}T_p} + \mathrm{C} \quad \text{(Eq.4)}$$

where β refers to the rate of heating, T indicates the peak temperatures in DSC curves and R stands for the gas constant. Figure 3(e) illustrates the dependence of $\ln(\beta/T_p^2)$ upon $1/T_p$. The value of E_a/R determines the slope of the

fitted line. Thus, the dehydrogenation activation energy is 72.04 kJ mol^{-1}, which is similar to the majority of the commonly occurring hydrides.

The thermodynamics of hydrogenation-dehydrogenation of the Mg-PdNi@rGN composite have been studied by PCT. The PCT curves were obtained at various temperatures of 280, 300, and 330 °C (Fig. S4(a) in the ESM). Each isotherm has a single obvious hydrogen absorption-desorption plateau that corresponds to the hydrogenation-dehydrogenation of magnesium. At 280 °C, the absorption-desorption plateau hydrogen pressures of MgH_2 are approximately 1.92 bar and 1.73 bar, respectively. While at 3000 °C, they are 3.11 bar and 2.98 bar, respectively; and at 603 K, they are 5.73 bar and 5.02 bar, respectively. The system demonstrates a reversible hydrogen capacity of 7.05 wt%, achieving 97.2% of the theoretical capacity of 7.25 wt%. The plateau pressures extracted from the PCT diagrams were used to construct Van't Hoff plots (Fig. S4(b) in the ESM), from which the enthalpy and entropy changes associated with hydrogenation and dehydrogenation were calculated using the van't Hoff equation.

$$\ln\left(\frac{P_{H_2}}{P^{\theta}}\right) = \frac{\Delta H_f}{RT} - \frac{\Delta S_f}{R} \quad \text{(Eq.5)}$$

The van't Hoff equations for Mg in the Mg-PdNi@rGN composite are obtained using linear fitting of ln$P$ *vs.* 1000/T.ln(P_{ab}) = -9.112/T+17.14 for hydrogen absorption of Mg and ln(P_{de}) = -9.004/T+17.07 for hydrogen desorption. The hydrogenation and dehydrogenation enthalpies of magnesium are determined to be -75.76 and +74.86 kJ mol^{-1} H_2, respectively, which are less than the as-received commercial magnesium (76 kJ mol^{-1} H_2). The result indicates that the addition of PdNi@rGN has a negligible effect on the reaction enthalpy of Mg. It can be concluded that the addition of PdNi@rGN has a minimal effect on thermodynamic performance, nevertheless, it significantly increases the kinetic attributes.

The HCS+MM sample Mg-PdNi@GN exhibits superior cyclic stability in hydrogenation-dehydrogenation tests, which is one of the most noteworthy findings of the current investigation. Isothermal cycling experiments were conducted at 523 K for 15 cycles, dehydrogenation was performed at 523 K for 30 min under 0.005 MPa H_2, and hydrogenation at 523 K for 10 min under 3.0 MPa H_2, with a 10 min evacuation between cycles to ensure complete dehydration. As shown in Fig. 4, the hydrogen storage capacity remains nearly constant over 15 cycles, decreasing only slightly from 6.77 to 6.68 wt% H_2. The first and last dehydrogenation kinetic profiles (Figs. 4(a) and 4(b)) further confirm that the Mg-PdNi@rGN composite maintains rapid hydrogen absorption and release throughout cycling. These results demonstrate not only the high structural stability of the composite but also the long-term catalytic robustness of the PdNi@rGN additive.

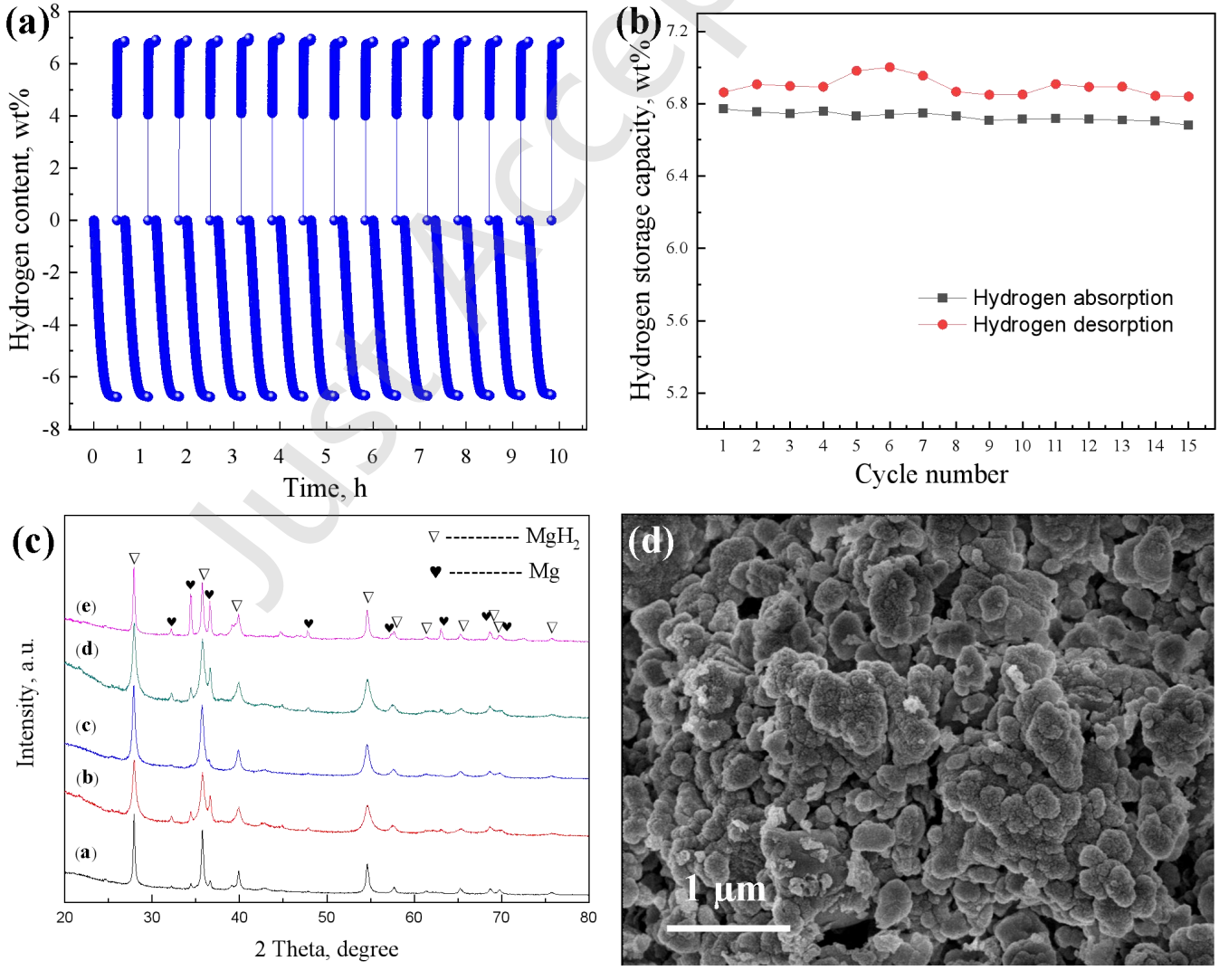

Figure 4 Isothermal hydrogenation and dehydrogenation cyclic kinetics curves of Mg–PdNi@rGN from the 1st to the 15th cycle at 300°C (a);Hydrogen

absorption/desorption capacity of Mg–PdNi@rGN as a function of cycle number (b);XRD patterns of Mg-PdNi@rGN composite after the 1st and 15th hydrogenation processes (c);FESEM images of Mg–PdNi@rGN after 15th cycles (d).

Figure 4(c) compares the XRD patterns of the Mg-PdNi@rGN composite in the hydrogenated state and after 15th hydrogenation–dehydrogenation cycles. The initial hydrogenated sample contains mainly MgH_2 and a small amount of MgO. ~~The relative intensity of MgO remains nearly unchanged, indicating the composite exhibits effective antioxidation.~~ Compared with the as-prepared sample, the diffraction peaks of MgH_2 in the cycled sample are sharper and more intense, reflecting grain growth and partial relaxation of lattice strain during cycling. FESEM images of Mg-PdNi@rGN after 15th cycles (Fig. 4(d)) reveal small particles with sizes of ~300-400 nm. Higher-magnification images show slightly increased particle size and agglomeration, attributed to volume expansion and local heating during cycling. The outstanding cyclic stability is attributed to the lamellar structure of graphene and the presence of Ni and Pd nanoparticles at the Mg/MgH_2 interfaces, which hinder boundary migration. Consequently, the PdNi@GN additive preserves both the catalytic activity and structural integrity of MgH_2 during repeated hydrogenation-dehydrogenation cycles.

XPS analysis was performed to probe the chemical states of catalyst components in both dehydrogenated and hydrogenated states (Figs. S5(a) and S5(b) in the ESM). It is valuable to study different components in the catalyst that have a different catalytic effect on the composite. The wide-scan spectra reveal Mg, O, and C as dominant surface elements, with lower concentrations of Ni (1.58 at.%) and Pd (1.39 at.%), suggesting surface segregation and selective oxidation. XPS wide scan spectrum for the HCS+MM sample Mg-PdNi@GN in the dehydrogenated (a) and hydrogenated (b) states. The peaks corresponding to Mg, O, and C are readily visible, although the Ni and Pd peaks are weaker. The finding implies that Mg surface segregation and selective oxidation occurred during the sample preparation phase, implying that oxidation occurred on the surface. The C 1s spectra of graphene show a binding energy decrease from 284.80 eV to 277.80 eV upon dehydrogenation, attributed to strong electronic interactions between graphene and Mg-H bonds or Ni/Pd nanoparticles. These interactions are believed to facilitate efficient hydrogenation and dehydrogenation of Mg, highlighting the synergistic catalytic effect of Pd, Ni, and graphene nanosheets.

Based on the above analysis, further DFT calculations were performed to elucidate the modifying effect of PdNi on the hydrogen storage properties of MgH_2, with the PdNi (1 1 1) crystal plane selected as the representative mode MgH_2 molecules were adsorbed at various sites on the PdNi surface, including atop Pd (Pd-top), atop Ni (Ni-top), and bridging Pd-Pd, Ni-Ni, and Pd-Ni sites (bridge-PdPd, bridge-NiNi, bridge-PdNi). The initial and optimized structures are shown in Figs. 5(a) and 5(b). The calculated adsorption energies, Mg-H1/H2 bond lengths, and bond angles are summarized in Table S1. After optimization, the Mg-H1/H2 bond lengths and H1-Mg-H2 bond angle of the free MgH_2 molecule were found to be 1.72/1.72 Å and 179.62°, respectively, consistent with previous reports [16], confirming the reliability of the MgH_2 structure. When adsorbed on Pd, Ni, or PdNi surfaces, the Mg-H bond lengths were elongated to 2.60-3.79 Å, and the bond angle decreased to 84.15-153.01°, indicating that all three surfaces facilitate the weakening of Mg-H bonds, accelerating bond cleavage and promoting the dehydrogenation of MgH_2. Notably, the most pronounced weakening effect was observed when MgH_2 was placed between Pd-Pd bonds (bridge-PdPd), where the bond lengths were uniformly stretched to 3.66/3.66 Å, and the bond angle reduced to 84.15°.

To further investigate the interaction between MgH_2 and the PdNi substrate in this configuration, additional calculations were performed. As shown in Figs. 5(c) and 5(d), a strong interaction exists between MgH_2 and PdNi, with significant electron accumulation near the H atoms of MgH_2 and electron depletion (blue region) around Mg. Moreover, the projected density of states (PDOS) for Mg, H, Pd, and Ni in this structure are presented in Figs. 5(e) and 5(f). Significant orbital hybridization occurs between Mg-s and Pd-d/Ni-d states in the energy range of -6 to -2 eV, indicating a strong interaction between Mg and PdNi, which weakens the Mg-H bond. These analyses demonstrate that the strong interaction between PdNi and MgH_2 induces electron redistribution around Mg and H, elongates Mg-H bonds, and reduces bond strength, thereby facilitating the dehydrogenation of MgH_2.

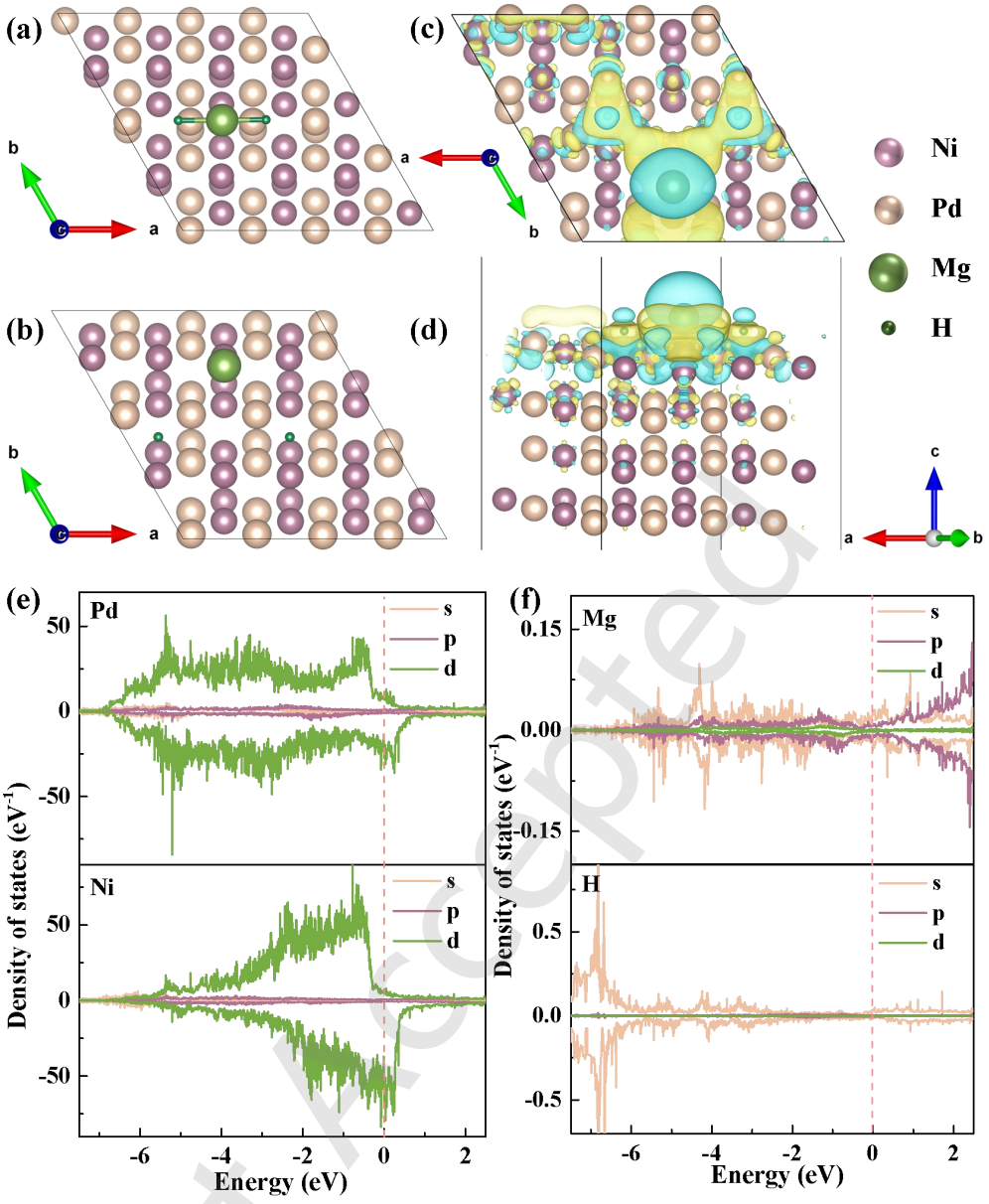

Figure 5 The initial (a) and optimized (b) absorption structures of the MgH_2 molecule on the Pd-Pd bridge of the PdNi. The top view (c) and side view (d) of the difference charge density for the MgH_2 molecule on the Pd-Pd bridge of the PdNi. The projected density of states of Pd(e) and Ni, and Mg (f) and H elements for the MgH_2 molecule on the Pd-Pd bridge of the PdNi.

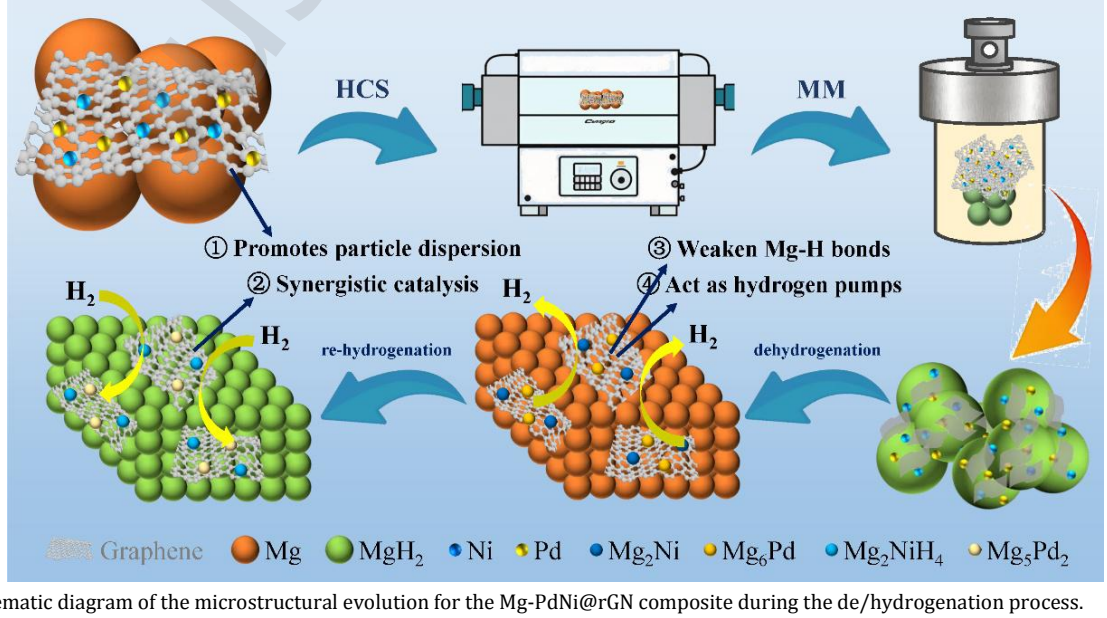

Figure 6 Schematic diagram of the microstructural evolution for the Mg-PdNi@rGN composite during the de/hydrogenation process.

To understand the synthesis mechanism of the HCS+MM sample Mg-PdNi@GN we demonstrate the preparation process of the composite including the synthesis process (HCS) and the grain refinement process (MM). During the HCS process, PdNi@GN catalysts were first mixed with Mg powder, followed by Mg volatilization to form nanoscale Mg particles, which subsequently reacted in situ with Pd and Ni nanoparticles to generate Mg_2NiH_4 and MgPd. The resulting nanoparticles were homogeneously distributed on the Mg/MgH_2 matrix, facilitated by the graphene nanosheets, which acted as structural supports for Pd and Ni, ensuring uniform dispersion of the ultrafine Mg_2NiH_4 and MgPd phases. Subsequent MM further refined the grain size and enhanced nanoparticle dispersion within the Mg/MgH_2 matrix. Thus, the combined HCS+MM approach provides a viable route to synthesize highly active, uniformly distributed catalysts, a prerequisite for efficient Mg hydrogen desorption. In the Mg-PdNi@GN composite, PdNi@GN nanoparticles cover the Mg surface, providing multivalent catalytic sites. Hydrogenation/dehydrogenation is a gas-solid reaction strongly influenced by the gas-solid interface. The hydrogenation/dehydrogenation process is a gas-solid reaction whose reaction rate is affected significantly by the gas-solid interface. A schematic diagram drawing the hydrogen pathways, porthole, and spillover effect of the catalysts in the system is also shown in Fig. 6, in situ formed Mg_6Pd and Mg_2Ni transform into MgPd and Mg2NiH4 upon hydrogenation, serving as "portholes" or pathways for H_2 release and recombination, similar to previously reported metal catalysts (Co, Cu, Mn, V). The following steps can be used to describe the composite's dehydrogenation process: (1) H- at the interface between MgH_2 and Mg_2NiH_4 gives e- to transform into high valence Pd and Ni; (2) Mg-H bond is broken onto MgPd and Mg2NiH4 nanoparticles prior to the Mg matrix; (3) Furthermore, Mg-H bond is weakened and dissociative H is produced and dehydrogenation reaction occurs; (4) H_2 molecule is recombined; (5) Mg may take M This will result in a significant reduction in the dehydrogenation barrier when compared to bulk Mg. The following is a detailed explanation of the hydrogen reaction. Mg_2NiH_4 NPS can hold up to 3.6 wt% H_2, and release it quickly. While MgPd nanoparticles facilitate reversible hydrogen desorption from MgH_2 through multiple disproportionation processes. (Eq.6-Eq.8):

$$MgPd + 5\ MgH_2 \leftrightarrow 0.5\ Mg_5Pd_2 + 3.5\ MgH_2 + 1.5\ H_2 \quad \text{(Eq.6)}$$

$$0.5\ Mg_5Pd_2 + 3.5\ MgH_2 \leftrightarrow Mg_{3.65}Pd + 2.35MgH_2 + 1.15\ H_2 \quad \text{(Eq.7)}$$

$$Mg_{3.65}Pd + 2.35\ MgH_2 \leftrightarrow Mg_6Pd + 2.35\ H_2 \quad \text{(Eq.8)}$$

As a result, Mg_2NiH_4 and MgPd NPS, as bifunctional portholes or pathways, prioritize hydrogen emission. These bifunctional portholes or channels are evenly dispersed on/in the MgH_2 matrix, allowing hydrogen diffusion to be facilitated. The hydrogen can escape from the sample through these portholes or channels, allowing hydrogen desorption at very low driving forces on the grain boundaries of MgH_2. In the case of hydrogenation, this is expected to result in greater hydrogen spillover as an anastrophic mechanism, with the conclusion that the spillover hydrogen is positioned at the two-phase boundary of MgH_2 and catalysts [60]. The Mg_2NiH_4 and MgPd NPs affect the connected MgH_2 neighbor and hence induce its hydrogen desorption, which is accompanied by a hydrogen porthole and spillover effect. Meanwhile, the dispersion state of the catalytic active sites is critical for the catalytic process to create new Mg nucleation sites. Furthermore, graphene nanoplates can operate as a thermal, electron-conductive, and hydrogen diffusion channel, allowing atomic hydrogen to diffuse from grain boundaries or acting as a hydride agglomeration inhibitor. Furthermore, the reduced graphene oxide acts as a protective agent, preventing bigger molecules like O_2 and H_2O from penetrating and considerably improving the chemical stability of Mg nanoparticles. As a result, it is possible that the dehydrogenation of MgH_2 was aided by the synergetic catalysis of Pd, Ni, and GN.

3 Conclusions

This work successfully prepared a graphene-supported Pd-Ni bimetallic catalyst modified Mg-PdNi@rGN composite material via Hydrogenation Combustion Synthesis (HCS) and Mechanical Milling (MM) techniques. This material demonstrates significantly enhanced hydrogen storage properties. The dehydrogenation onset temperature of the composite is reduced to 140 °C, with a peak temperature of only 256.9 °C (94.7 °C lower than pure MgH_2). The dehydrogenation activation energy is decreased to 70.5 kJ mol^{-1}. Furthermore, the composite exhibits highly efficient low-temperature kinetics: it achieves a saturated capacity of 6.46 wt% within 100 seconds at a low temperature of 100°C, outperforming the single-component Mg-Ni@rGN and Mg-Pd@rGN systems. Additionally, it completes dehydrogenation of 6.70 wt% in 400 s at 300°C, and can still release 0.65 wt% after 1800 s at 200 °C. Notably, after 15 high-temperature cycles at 523 K, the composite maintains a remarkable capacity retention rate of 98.95 % (with only 0.07 wt% decay), confirming the stability of the PdNi@rGN catalytic interface. Density Functional Theory calculations and microstructural characterization reveal that the PdNi nanocatalyst induces electron redistribution in the Mg-H bond, weakening the bond strength and facilitating H dissociation. Moreover, Mg_2NiH_4 and MgPd nanoparticles are in-situ generated during cycling, acting as hydrogen storage intermediates. These intermediates, synergistically catalyzed by the "Hydrogen Channeling Effect" and "Hydrogen Spillover Effect", along with the graphene support functioning as both a hydrogen transport pathway builder and an anti-agglomeration barrier, create a triple mechanism that collectively promotes the reversible hydrogen storage of MgH_2.

Electronic Supplementary Material: Supplementary material (XRD patterns, particle size analysis, SEM image, EDS mappings, TEM images, SAED pattern, TPD-MS curves, TPD profiles, PCT curves, van't Hoff plots, and XPS survey spectras for Mg-PdNi@rGN) is available in the online version of this article at https://doi.org/10.26599/NR.2026.94908502.

Data availability

All data needed to support the conclusions in the paper are presented in the manuscript and/or the Electronic

Supplementary Material. Additional data related to this paper may be requested from the corresponding author upon request.

Acknowledgements

This work was funded by the Strategic Priority Research Program of the Chinese Academy of Sciences (XDA0400304), National Natural Science Foundation of China (52401262, 52271212, 52301295, 52501270), the Basic Research Program of Jiangsu (BK20220156), Science and Technology Development Plan of Jilin Province (20230201140GX), Youth Innovation Promotion Association CAS (2022225), Science and Technology Development Plan of Changchun (2024GD01).

Declaration of competing interest

All the contributing author(s) report(s) no conflict of interests in this work.

Author contribution statement

B. Z. Z.: Data curation, writing – original draft, resources. Y. L.: Data curation, investigation, visualization. J. G.: investigation, validation. H. G. G.: Data curation, investigation, validation. X. H. S.: Writing – review & editing. Q. Y. S.: Data curation. X. X. W.: Data curation. R. K. H.: Data curation. Y. F. L.: Data curation. Q. S. W.: Investigation. C. Y. Z.: visualization. J. G. Y.: Writing – review & editing, resources, supervision, validation. All the authors have approved the final manuscript.

Informed consent

Not applicable.

Ethics statement

Not applicable.

Use of AI statement

None.

References

[1] Zheng, X.; Wang, T. D.; Lu, Y.; Hao, J. C.; Gao, G. H.; Wu, G. M.; Zhuang, Z. C.; Zhu, H. Navigating Complexity to Design Nanostructured High-Entropy Alloy Catalysts. *Adv. Energy Mater.* **2025**, e04545.

[2] Li, J. L.; Gan, T.; Yu, R. H.; Cai, J.; Zhuang, Z. C.; Zhu, H. Cooling Crystallization at Solid Interfaces en Route to a Janus Nanocatalyst. *Adv. Mater.* **2025**, e12893.

[3] Li, M. L.; Wang, Y. F.; Zhang, H.; Zhuang, Z. C.; Li, J. F. In situ Raman spectroscopy studies of single-atom catalysis. *Appl. Catal. A-Gen.* **2025**, *708*, 120600.

[4] Yang, X. H.; Yang, J. R.; Zheng, X. B.; Dou, Y. H.; Li, H. T.; Zhang, Y.; Li, Y. F.; Wang, D. S.; Yu, B.; Zhuang, Z. C. Enzyme-Mimetic Single-Atom Catalyst Design for Green Ammonia Synthesis. *Adv. Energy Mater.* **2025**, *15*, 2501867.

[5] Lang, Z. Q.; Zhuang, Z. C.; Song, G. L.; Guo, L. F.; Wang, S. H.; Liao, X. P.; Wu, P. P.; Li, Y. X.; Liu, Y. L.; Liu, N. Y.; Zhu, Y. X.; Wang, D. S.; Zhao, C.; Li, H. T. Corrosion-Regulated Surface Reconstruction for High-Performance Oxygen Evolution Electrocatalysts. *ACS Nano*. **2025**, *19*, 31065–31076.

[6] Shi, J. D.; Cheng, Y. X.; Wang, T.; Peng, Y. H.; Lin, X. L.; Tang, B.; Feng, M. B.; Zhuang, Z. C.; Sun, Y. M.; Yu, X.; Xu. Z. C. J. Site-Specific Spin State Modulation in Spinel Oxides for Enhanced Nonradical Oxidation. *Angew. Chem. Int. Ed.* **2025**, *64*, e202504189.

[7] Ren, P. F.; Gan, T.; Cai, J.; Hao, J. C.; Zhuang, Z. C.; Jin, C. Y.; Zhang, W. C.; Du, M. L.; Zhu, H. High-Entropy Environments Enable Metal Surface-Catalyzed Nucleophilic Electrooxidation. *Angew. Chem. Int. Ed.* **2025**, *64*, e202502776.

[8] Zhou, J. Y.; Qin, L. Y.; Fang, L.; Zhu, X. J.; Wang, L. L.; Zhuang, Z. C. 2M-phase transition metal dichalcogenides: From fundamental to application. *Nano Res.* **2025**, *18*, 94907312.

[9] Lang, Z. Q.; Wang, X. X.; Jabeen, S.; Cheng, Y. Y.; Liu, N. Y.; Liu, Z. H.; Gan, T.; Zhuang, Z. C.; Li, H. T.; Wang, D. S. Destabilization of Single-Atom Catalysts: Characterization, Mechanisms, and Regeneration Strategies. *Adv. Mater*. **2025**, *37*, 2418942.

[10] Hao, J. C.; Wang, T. D.; Cai, J.; Gao, G. H.; Zhuang, Z. C.; Yu, R. H.; Wu, J. S.; Wu, G. M.; Lu, S. L.; Wang, X. F.; Du, M. L.; Wang, D. S.; Zhu, H. Suppression of Structural Heterogeneity in High-Entropy Intermetallics for Electrocatalytic Upgrading of Waste Plastics. *Angew. Chem. Int. Ed.* **2025**, *64*, e202419369.

[11] Zhuang, Z. C.; Wang, D. S. Advancing hydrogen energy through enzyme-mimetic electrocatalysis. *Front. Energy* **2025**, *19*, 563–567.

[12] Muhammed, N. S.; Gbadamosi, A. O.; Epelle, E. I.; Abdulrasheed, A. A.; Haq, B.; Patil, S.; Al-Shehri, D.; Kamal, M. S. Hydrogen production, transportation, utilization, and storage: Recent advances towards sustainable energy. *J. Energy Storage*. **2023**, *73*, 109207.

[13] Sun, H.; Wang, Z. Y.; Meng, Q.; White, S. Advancements in hydrogen storage technologies: Enhancing efficiency, safety, and economic viability for sustainable energy transition. *Int. J. Hydrogen Energy*. **2025**, *105*, 10–22.

[14] Karayel, G. K.; Javani, N.; Dincer, I. A comprehensive assessment of energy storage options for green hydrogen. *Energy Convers. Manage*. **2023**, *291*, 117311.

[15] Naseem, K.; Qin, F.; Khalid, F.; Suo, G. Q.; Zahra, T.; Chen, Z. J.; Javed, Z. Essential parts of hydrogen economy: Hydrogen production, storage, transportation and application. *Renew. Sustain. Energy Rev.* **2025**, *210*, 115196.

[16] Wang, L.; Zhao, B. Z.; Liu, J. C.; Yuan, J. G.; Zhu, Y. F.; Liu, B. G.; Wu, Y.; Li, L. Q.; Cheng, Y.; Zhou, S. X. Effect of Ti-EG-Ni Dual-Metal Organic Crystal-Derived TiO2/C/Ni on the Hydrogen Storage Performance of MgH_2. *ACS Appl. Mater. Interfaces*. **2025**, *17*, 15274–15286.

[17] Zhou, M. H.; Xue, Y. Q.; Ge, F.; Li, J.; Xia, H. H.; Xu, J. M.; Zhao, J.; Chen, C. Z.; Jiang, J. C. MOF-derived NiM@C catalysts (M = Co, Mo, La) for in-situ hydrogenation/hydrodeoxygenation of lignin-derived phenols to cycloalkanes/cyclohexanol. *Fuel*. **2022**, *329*, 125446.

[18] Zhou, D. S.; Sun, H. F.; Guo, S. H.; Zhao, D. L.; Li, J.; Zhang, Y. H. Hydrogen storage properties of mg-based alloys modified with metal-organic frameworks and carbon-based porous materials: a review and summary. *Int. J. Hydrogen Energy*. **2024**, *57*, 1373–1388.

[19] Huang H, Xu T, Chen J, Yuan J, Yang W, Liu B, Zhang B, Wu Y. Enhanced catalysis of Pd single atoms on Sc_2O_3 nanoparticles for hydrogen storage of MgH_2. *Chem. Eng. J.* **2024**, *483*, 149434.

[20] Ding, Z.; Li, Y. T.; Yang, H.; Lu, Y. F.; Tan, J.; Li, J. B.; Li, Q.;

Chen, Y. A.; Shaw, L. L. Pan, F. S. Tailoring MgH_2 for hydrogen storage through nanoengineering and catalysis. *J. Magnes. Alloy.* **2022**, *10(11)*, 2946-2967.

[21] Li, Q.; Lu, Y. F.; Luo, Q.; Yang, X. H.; Yang, Y.; Tan, J.; Dong, Z. H.; Dang, J.; Li, J. B.; Chen, Y.; Jiang, B.; Sun, S. H.; Pan, F. S. Thermodynamics and kinetics of hydriding and dehydriding reactions in Mg-based hydrogen storage materials. *J. Magnes. Alloys.* **2021**, *9*, 1922–1941.

[22] Ren, L.; Li, Y. H.; Zhang, N.; Li, Z.; Lin, X.; Zhu, W.; Lu, C.; Ding, W. J.; Zou, J. X. Nanostructuring of Mg-Based Hydrogen Storage Materials: Recent Advances for Promoting Key Applications. *Nano-Micro Lett.* **2023**, *15*, 93.

[23] Zhang, J. R.; Liu, M. L.; Qi, J. C.; Lei, N.; Guo, S. R.; Li, J. F.; Xiao, X. Z.; Ouyang, L. Z. Advanced Mg-based materials for energy storage: fundamental, progresses, challenges and perspectives. *Prog. Mater. Sci.* **2025**, *148*, 101381.

[24] Shen, S.Y.; Li,Y.A.; Ouyang, L.Z.; Zhang,L.; Zhu,L.; Liu, Z.W. V-Ti-Based Solid Solution Alloys for Solid-State Hydrogen Storage. *Nano-Micro Lett.* **2025**, *17(1)*: 175

[25] Shen, S. Y.; Liao, W. F.; Cao, Z. J.; Liu, J. W.; Wang, H.; Ouyang, L. Z. Enhanced hydrogen storage properties of MgH_2 with the co-addition of $LiBH_4$ and YNi_5 alloy. *Journal of Materials Science & Technology*. **2024**, *178,* 90-99

[26] Ding, Z.; Li, H.; Shaw, L. L. New insights into the solid-state hydrogen storage of nanostructured $LiBH_4$-MgH_2 system. *Chem. Eng. J.* **2020**, *385*, 123856.

[27] Qiu, J. Q.; Wan, H. Y.; Li, Y. T.; Guo, Z. Y.; Ding, Z.; Chen, Y, A.; Pan, F. S. Multiscale mechanistic insights into Er-driven phase reconfiguration and hydrogen diffusion in Mg–Ni alloys. Nano.Mater. Sci., in press, DOI: 10.1016/s2589965125001291.

[28] Li, Y. T.; Ding, Z.; Jiang, H.; Lin, G.; Li, S. Y.; Du W. J.; Chen, Y. A.; Shaw, L. L.; Pan, F. S. Spatially Programmed Confinement Catalysis Enables High-Performance Magnesium Hydrogen Storage. *Nano. Lett.* 2025, *25(48)*, 16801-16808.

[29] Guan, H. T.; Liu, J.; Sun, X.; Lu, Y. F.; Wang, H. Y.; Luo, Q.; Li, Q.; Pan, F. S. Titanium–Nickel Dual Active Sites Enabled Reversible Hydrogen Storage of Magnesium at 180 °C with Exceptional Cycle Stability. *Adv. Mater.* **2025**, *2500178.*

[30] Liu, Z. Q.; Ning, H.; Liu, R. J.; Ding, S. Z.; Yang, J. K.; Tan, Y. X.; Fan, Y.; Li, R. H.; Qing, P. L.; Liu, H. Z.; Guo, J.; Lan, Z. Q. Fabrication of V_2O_3-TiO_2-rGO ternary heterojunction composite to enhance the hydrogen storage performance of MgH_2. *Chem. Eng. J.* **2024**, *499*, 155877.

[31] Yuan, Z. L.; Wang, Y. H.; Zhang, X. X.; Guan, S. Y.; Wang, X. J.; Ji, L. Q.; Peng, Q. M.; Han, S. M.; Fan, Y. P.; Liu, B. Z. Catalytic effects of V- and O-species derived from PrF_3/V_2C for efficient hydrogen storage in MgH_2. *Nano Res.* **2024**, *17*, 7117–7125.

[32] Lv, M. L.; Zheng, J. G.; Xia, A.; Zhang, Q. B.; Ma, Z. X.; Su, C.; Ge, L. Bimetallic Ti_2NbC_2 MXene as an efficient catalyst for reversible hydrogen storage in magnesium hydride. *Rare Met.* **2025**, *44*, 2489–2501.

[33] Li, Y. H.; Ren, L.; Yao, Y. Y.; Zhao, Y. Y.; Xu, H.; Li, Z.; Li, Z.; Dai, X. H.; Tian, Y. H.; Cao, S. S.; Lin, X.; Ye, C. N.; Züttel, A.; Zou, J. X. A Single‐Atom Interface Engineering Strategy to Promote Hydrogen Sorption Performances of Magnesium Hydride. *Adv. Funct. Mater.* **2025**, *35*, 2417915.

[34] Li, S.; Zhang, L. T.; Wu, F. Y.; Jiang, Y. Q.; Yu, X. B. Efficient catalysis of FeNiCu-based multi-site alloys on magnesium-hydride for solid-state hydrogen storage. *Chin. Chem. Lett.* **2025**, *36*, 109566.

[35] Xian, K. C.; Wu, M. H.; Gao, M. X.; Wang, S.; Li, Z. L.; Gao, P. Y.; Yao, Z. H.; Liu, Y. F.; Sun, W. P.; Pan, H. G. A Unique Nanoflake-Shape Bimetallic Ti–Nb Oxide of Superior Catalytic Effect for Hydrogen Storage of MgH_2. *Small.* **2022**, *18*, 2107013.

[36] Guan, H. T.; Liu, J.; Sun, X.; Lu, Y. F.; Wang, H. Y.; Luo, Q.; Li, Q.; Pan, F. S. Titanium–Nickel Dual Active Sites Enabled Reversible Hydrogen Storage of Magnesium at 180 °C with Exceptional Cycle Stability. *Adv. Mater.* **2025**, *37*, 2570178.

[37] Xu, N.; Wang, K. W.; Zhu, Y. F.; Zhang, Y. PdNi Biatomic Clusters from Metallene Unlock Record - Low Onset Dehydrogenation Temperature for Bulk-MgH_2. *Adv. Mater.* **2023**, *35*, 2303173.

[38] Xu, N.; Zhou, H. R.; Zhang, M. Q.; Ye, Y. C.; Wang, K. W.; Zhou, Y. T.; Zhu, Y. F.; Zhang, Y. Synergistic effect of Pd single atoms and clusters on the de/re-hydrogenation performance of MgH_2. *J. Mater. Sci. Technol.* **2024**, *191*, 49–62.

[39] Gao, H. G.; Song, M. C.; Zhao, B. Z.; Liu, J. C.; Shi, R.; Liu, Y. N.; Hu, X. H.; Zhu, Y. F. Assisting molybdenum trioxide catalysis by engineering oxygen vacancy for enhancing hydrogen storage performance of magnesium hydride. *J. Colloid Interf. Sci.* **2025**, *678*, 343–352.

[40] Zhu, Y. F.; Qin, Z. K.; Shi, X. B.; Ding, X. L.; Dao, V.-D.; Li, Y. T. Size-dependent activity modulation of supported Ni nanocatalysts for efficient solid-state hydrogen storage in magnesium. *Chem. Eng. J.* **2024**, *498*, 155285.

[41] Dai, Z. Y.; Zhang, B.; Kimura, H.; Xiao, L. R.; Liu, R. H.; Ni, C.; Hou, C. X.; Sun, X. Q.; Zhang, Y. P.; Yang, X. Y.; Yu, R. H.; Du, W.; Xie, X. B. Vermiform Ni@CNT derived from one-pot calcination of Ni-MOF precursor for improving hydrogen storage of MgH_2. *Trans. Nonferrous Met. Soc. China.* **2024**, *34*, 2629–2644.

[42] Zhang, X.; Liu, Y. F.; Ren, Z. H.; Zhang, X. L.; Hu, J. J.; Huang, Z. G.; Lu, Y. H.; Gao M. X.; Pan, H. G. Realizing 6.7 wt% reversible storage of hydrogen at ambient temperature with non-confined ultrafine magnesium hydride. *Energy Environ. Sci.* **2021**, *14*, 2302-2313.

[43] Li, Y. H.; Ren, L.; Yao, Y. Y.; Zhao, Y. Y.; Xu, H.; Li, Z.; Li, Z.; Dai, X. H.; Tian, Y. H.; Cao, S. S.; Lin, X.; Ye, C. N.; Züttel, A.; Zou, J. X. A Single-Atom Interface Engineering Strategy to Promote Hydrogen Sorption Performances of Magnesium Hydride. *Adv. Funct. Mater.* **2025**, *35*, 2417915.

[44] Jiang, H.; Ding, Z.; Li, Y. T.; Lin, G.; Li, Y. S.; Du, W. J.; Chen, Y. A.; Shaw, L. L.; Pan, F. S. Hierarchical interface engineering for advanced magnesium-based hydrogen storage: synergistic effects of structural design and compositional modification. *Chem. Sci.* **2025**, *16(18)*, 7610-7636.

[45] Tang, Q. K.; Liu, J. C.; Shi, R.; Zhu, Y. F.; Zhang, J. G.; Liu, Y. N.; Wang, J.; Zhang, Y.; Hu, X. H.; Liu, Z. B.; Li, L. Q. Synthesis of highly stable Ni nanoparticles via electrostatic self-assembly for enhanced hydrogen storage of MgH_2. *Rare Met.* **2024**, *43*, 4356–4366.

[46] Xie, X. B.; Xiao, L. R.; Kimura, H.; Wu, P.; Du, W.; Wu, Y. Effects of layered walnut NiS@NTA on hydrogen storage performance of MgH_2. *Sep. Purif. Technol.* **2025**, *359, 130837.*

[47] Huang, H.; Xu, T.; Chen, J.; Yuan, J.; Yang, W.; Liu, B.; Zhang, B.; Wu, Y. Enhanced catalysis of Pd single atoms on Sc_2O_3 nanoparticles for hydrogen storage of MgH_2. *Chem. Eng. J.* **2024**, *483*, 149434.

[48] Duan, C. W.; Wu, J. H.; Liang, P. Q.; Wang, H. M.; Qu, T.; Fan, Y.

C.; Su, Y. H.; Su, Z. H.; Hu, L. X.; Wu, Y. CNTs-Pd as Efficient Bidirectional Catalyst for Improving Hydrogen Absorption/Desorption Kinetics of Mg/MgH_2. *Energy Fuels*. **2024**, *38*, 8979–8991.

[49] Yin, X. C.; Sun, G.; Song, A. L.; Wang, L. X.; Wang, Y. Z.; Dong, H. F.; Shao, G. J. A novel structure of Ni-(MoS_2/GO) composite coatings deposited on Ni foam under supergravity field as efficient hydrogen evolution reaction catalysts in alkaline solution. *Electrochim. Acta*. 2**017**, *249*, 52–63.

[50] Liu, G. H.; Wang, L. X.; Hu, Y. W. T.; Sun, C. H.; Leng, H. Y.; Li, Q.; Wu, C. Z. Enhanced catalytic effect of TiO_2@rGO synthesized by one-pot ethylene glycol-assisted solvothermal method for MgH_2. *J. Alloys Compd*. **2021**, *881*, 160644.

[51] Gao, D. Q.; Wu, F. Y.; Zhang, Z.; Lu, Z. C.; Zhou, R.; Zhao, H.; Zhang, L. T. Graphene-loaded nickel-vanadium bimetal oxides as hydrogen pumps to boost solid-state hydrogen storage kinetic performance of magnesium hydride. *Trans. Nonferrous Met. Soc. China*. **2024**, *34*, 2645–2657.

[52] Huang H, Li X, Yao M, Yuan J, Chen J, Xu T, Duan W, Li Y, Liu B, Zhang B, Wu Y. Graphene‐Supported Ni/Sc_2O_3 Nanoheterostructures: Oxygen Vacancy‐Enhanced Catalysis for High‐Performance Mg‐Based Hydrogen Storage. *Adv Funct Materials.* 2025，31108.

[53] Zhang, K.; Chang, Y.; Lei, J. J.; Chen, J.; Si, T. Z.; Ding, X. L.; Cui, P.; Li, H. W.; Zhang, Q. A.; Li, Y. T. Synergy of inside doped metals-Outside coated graphene to enhance hydrogen storage in magnesium-based alloys. *J. Magnes. Alloys*. **2024,** *12*, 2462–2471.

[54] Bu, F. Q.; Wajid, A.; Yang, N.; Gu, M. Y.; Zhao, X. W.; Huang, L.; Ji, X.; Ding, S. J.; Cheng, Y. H.; Zhang, J. Y. Fabrication of amorphous TiO_2 hydrogen channels and graphene wrappers to enhance the hydrogen storage properties of MgH_2 with extremely high cycle stability. *J. Mater. Chem. A* **2024**, *12*, 12190–12197.

[55] Zhu, X. Q.; Yang, M. J.; Luo, M. M.; Wang, Y. H.; Li, H.; Ding, J. T.; Ma, L. Q. Enhanced dehydrogenation properties of MgH_2 by the synergetic effects of transition metal carbides and graphene. *Nanotechnology*. **2023**, *34*, 325704.

[56] Dong, S.; Liu, H.; Liu, X. Y.; Li, C. Q.; Gao, Z. Y.; Liu, B. G.; Yang, W. J.; Wu, Y. Facile dehydrogenation of MgH_2 enabled by γ-graphyne-based single-atom catalyst. *J. Energy Storage*. **2023**, *74*, 109484.

[57] Bu, F. Q.; Wajid, A.; Yang, N.; Gu, M. Y.; Zhao, X. W.; Huang, L.; Ji, X.; Ding, S. J.; Cheng, Y. H.; Zhang, J. Y. Fabrication of amorphous TiO_2 hydrogen channels and graphene wrappers to enhance the hydrogen storage properties of MgH_2 with extremely high cycle stability. *J. Mater. Chem. A*. **2024**, *12*, 12190–12197.

[58] Liu, G.; Wang, Y. J.; Qiu, F. Y.; Li, L.; Jiao, L. F.; Yuan, H. T. Synthesis of porous Ni@rGO nanocomposite and its synergetic effect on hydrogen sorption properties of MgH_2. *J. Mater. Chem*. **2012**, *22*, 22542.

[59] Jia, Y.; Cheng, L. N.; Pan, N.; Zou, J.; Lu, G. Q.; Yao, X. D. Catalytic De/Hydrogenation in Mg by Co‐Doped Ni and VO_x on Active Carbon: Extremely Fast Kinetics at Low Temperatures and High Hydrogen Capacity. *Adv. Energy Mater*. **2011**, *1*, 387–393.

[60] Qiao, W. F.; Liu, W. Q.; Yin, D. M.; Ding, N.; Liu, Y. F.; Sun, H. T.; Wang, Y.; Wang, Z. M.; Wang, C. L.; Wang, L. M.; Yuan, J. G.; Yong Cheng, Y. Ni-induced electronic modulation and structural resilience in TiMn-based AB2-type alloys for ultra-stable hydrogen storage. *Nano Research Energy*. **2026**, *5*, e9120216.

Electronic Supplementary Material

Enhanced hydrogen storage kinetics of magnesium hydride enabled by graphene-supported Pd–Ni bimetallic nanocatalysts

Baozhou Zhao[1] ✉, Yuan Li[2,3], Haiguang Gao[4], Jia Guo[1], Xiaohao Shi[1], Qingyun Shi[2,3], Xinxin Wang[2,3], Runkuo Han[2,3], Yufei Liu[2,3], Qingshuang Wang[5], Chaoyue Zhao[6], and Jianguang Yuan[2,3] ✉

[1] *School of Medical and Health Engineering,Changzhou University, Changzhou 213164, China*
[2] *State Key Laboratory of Rare Earth Resource Utilization, Changchun Institute of Applied Chemistry, Chinese Academy of Sciences, Changchun 130022, China*
[3] *School of Applied Chemistry and Engineering, University of Science and Technology of China (USTC), Hefei 230026, China*
[4] *Jiangsu Key Laboratory of Advanced Catalytic Materials and Technology, School of Petrochemical Engineering, Changzhou University, Changzhou 213164, China*
[5] *College of Life Science and Technology, Changchun University of Science and Technology, Changchun 130022, China*
[6] *Jilin JiEn Nickel Industry Co., Ltd., Jilin 132311, China*

✉ Address correspondence to Jianguang Yuan, jgyuan@ciac.ac.cn; Baozhou Zhao, zbzzsj@cczu.edu.cn

Supporting information to https://doi.org/10.26599/NR.2026.94908502

Section S1 Experimental

S1.1 Preparation of PdNi@GN catalyst

Original powders of Mg (99.72 wt.% in purity and <100 μm in size), $PdCl_2$ (AR, 99 wt.% in purity), $Ni(NO_3)2{\cdot}6H_2O$ (AR, 99 wt.% in purity), ethylene glycol (CP, 98 wt.% in purity) and graphene nanosheets (>97 wt.% in purity and 40-60 nm in external diameter) were commercially gotten.

The surface of graphene nanosheets was treated to ensure functionalization. graphene nanosheets were added to 50 ml concentrated nitric acid under stirring in an oil bath, with an increase in the temperature to 413 K. It was further refluxed and stirred for 6 h to remove impurities, and washed with distilled water till the pH value of the rinsed solution reached around 7, and finally dried under vacuum.

Ni@GN (mass ratio =3:4) was synthesized by a chemical reduction method of an annealing process. graphene nanosheets and $NiNO_3{\cdot}6H_2O$ were dispersed into ethyl alcohol by ultrasonic vibration for 1h, followed by drying in blowing dry oven at 358 K for 6h. Finally, the mixture was heat-treated at 673 K and held for 4 h in a tube furnace under Ar atmosphere. It was then heated up to 723 K and held for 4 h under H_2 atmosphere to ensure complete reduction of Ni. The sample was labeled as 3Ni@4GN.

PdNi@GN (mass ratio =3:3:4) was synthesized by a solution chemical reduction method. The as-synthesized Ni@GN was dispersed into ethylene glycol by ultrasonic vibration for 1h. Further, the required proper amount of aqueous solution of $PdCl_2$ was added to the solution under the condition of magnetic stirring for 4h. The pH of the entire solution was adjusted to more than 10 by adding NaOH (2.5 M), and the solution was refluxed and magnetic stirred in an oil bath at 383 K for 6 h to ensure complete reduction of Pd. In this reaction as the formula (1), ethylene glycol acted as a reducing, stabilizing, and dispersing agent. Finally, the suspension was filtered and the solid was washed with distilled water repeatedly until neutral and dried in blowing dry oven at 358 K. The sample was labeled as PdNi@GN.

$$x\,Pd^{2+} + x\,H_2(HO)CC(OH)H_2 \xrightarrow{NaOH/\Delta} Pd_x - colloids + x\,(HO)CC(OH)H_2 + 2x\,H^+ \quad \text{(Eq.1)}$$

S1.2 Preparation of Mg-PdNi/GN composite

The as-synthesized PdNi@GN and Mg mixed in a certain molar ratio (5:95) were homogenized by ultrasonic vibration in acetone for 30 min. After being completely dried in air, the powders were directly used for HCS. During the HCS process, the samples were first heated up to 853 K at a heating rate of 10 K/min under 2 MPa hydrogen atmosphere and kept at that temperature for 1 h. It was then cooled down to 613 K and held for 4 h. Finally, the sample was cooled down to room temperature. Afterward, the HCS product was mechanically milled for 10 h in a stainless steel vial with stainless steel balls under H_2 atmosphere with the ball to powder ratio of 30:1. MM was conducted with a 400 r/min milling rate by a planetary milling apparatus. The as-prepared HCS products were denoted as Mg-PdNi@GN. To verify the bimetal synergetic catalysis in this study, three samples of Mg-Pd@GN, Mg-Ni@GN, Mg-GN and Mg were prepared by the above- mentioned method.

Section S2 Sample characterization

The microstructures of the catalysts, HCS and HCS + MM products were examined by means of X-ray diffraction (XRD) with Cu-K_α radiation (40 kV and 35 mA), scanning electron microscopy (SEM, JEOL JSM-6360LV) and high-resolution transmission electron microscope (HRTEM, JEM-2010 UHR). X-ray photoelectron spectroscopy (XPS) was carried out in a Perkin Elmer PHI 550 multi-technique spectrometer with the electron gun Perkin Elmer PHI 25-270AR precision electron analyzer. Data acquisition took place in the constant energy analyzer mode with a pass energy of $\triangle E$ = 50 eV and Al K_α radiation from a monochromatic aluminum X-ray source. The sample was mixed with silicon dioxide and tableted before testing. The binding energy calibration was performed on the silicon Si 2p peak with the energy of 103.4 eV. The software Rietica was used for the quantitative phase analysis of the HCS product based on the Rietveld method. The average grain sizes of the main phase MgH_2 in the composites were estimated from the XRD patterns according to scherrer's equation:

$$D\,\beta\,cos\theta = 0.9\,\lambda \quad \text{(Eq.2)}$$

where D is the grain size, λ is the X-ray wavelength of 0.154 nm, β is the full width at half maximum of the diffraction peak and θ is the Bragg angle. Samples of TEM characterization were prepared by ultrasonic shaking of the powder in ethanol and drying it on a copper grid with a holey carbon foil.

The hydrogen storage properties of the HCS + MM products were measured by a Sieverts type apparatus (GRC, Advanced Materials Co.). About 0.5 g of the powders was loaded into a stainless steel sample chamber in the glove box filled with argon. Since the HCS + MM products were hydrides, they were dehydrogenated completely by evacuating upon being heated to 603 K at a heating rate of 5 K/min prior to the hydriding kinetics measurement. Then, the hydriding kinetics at different temperatures was measured under the initial hydrogen pressure of 3.0 MPa. The dehydriding kinetics was measured under vacuum at 473 K, and 0.005 MPa hydrogen pressure at temperatures higher than 523 K.

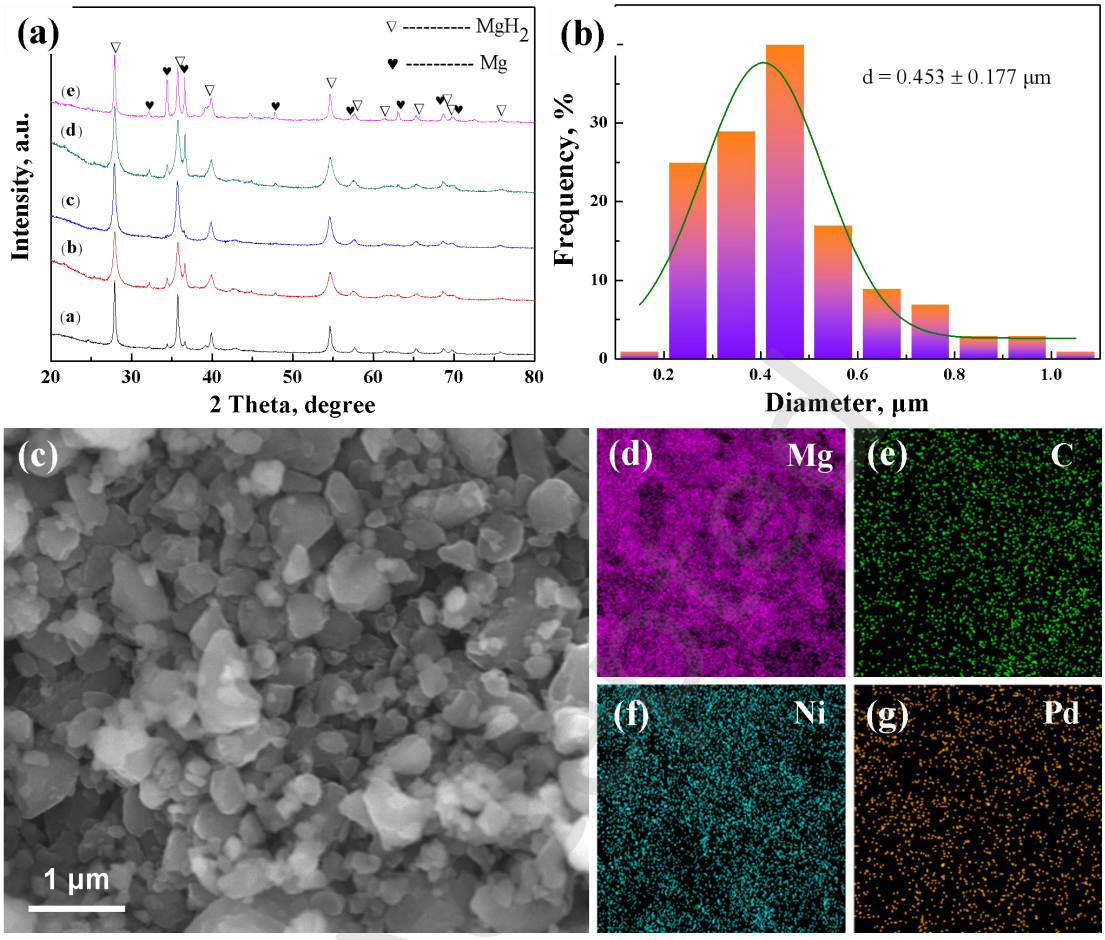

Figure S1 XRD patterns of Mg-PdNi@rGN, Mg-Ni@rGN, Mg-Pd@rGN, Mg-rGN, and Mg (a),particle size analysis (b),FESEM image (c) and EDS mappings of Mg-PdNi@rGN (d-g).

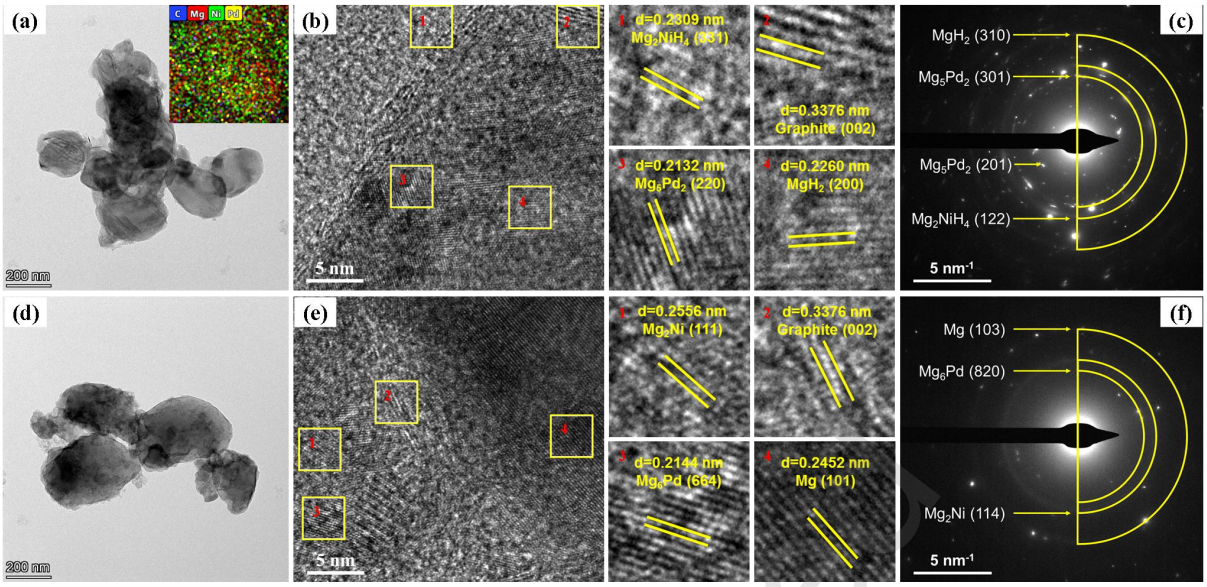

Figure S2 TEM images of the hydrogenated (a-b) and as-milled Mg-PdNi@rGN (d-e). SAED pattern of hydrogenated (c) and as-milled Mg-PdNi@rGN (f).

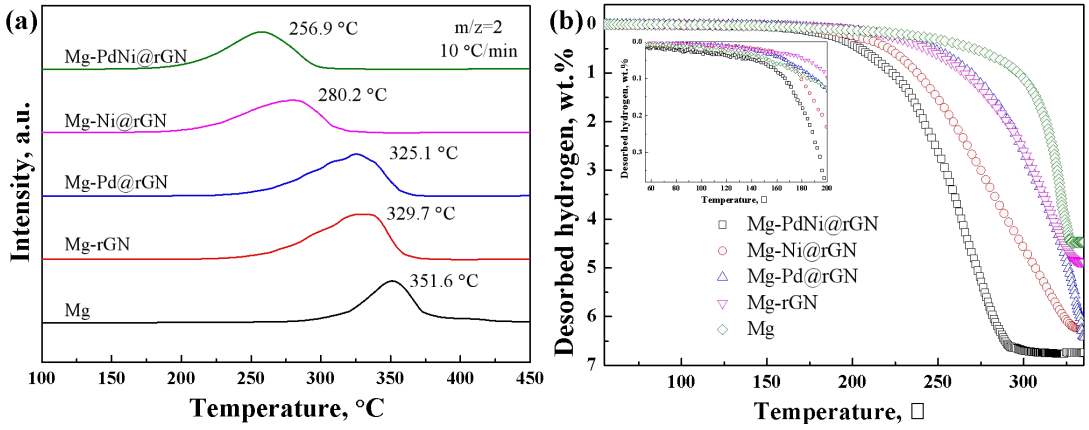

Figure S3 TPD-MS curves (a) and TPD profiles (b) for the HCS+MM samples at a heating rate of 10 °C min^{-1}.

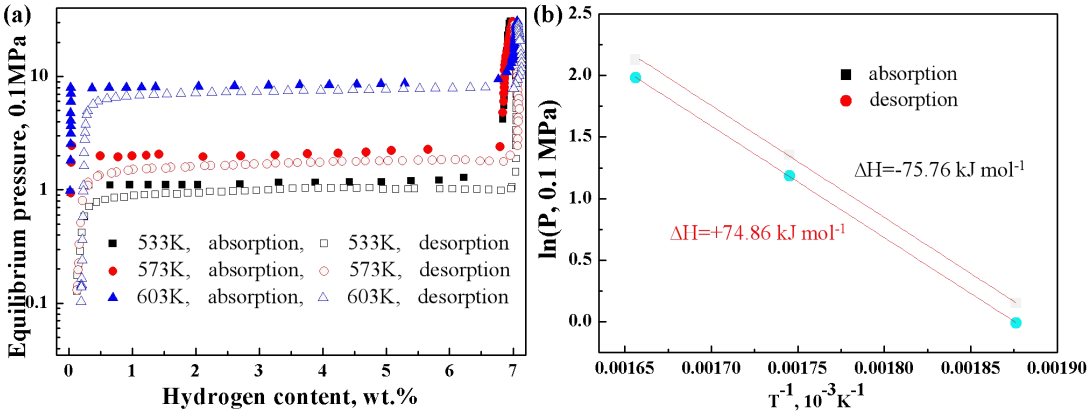

Figure S4 PCT curves (a) and van't Hoff plots (b) of the HCS+MM Mg-PdNi@rGN composite.

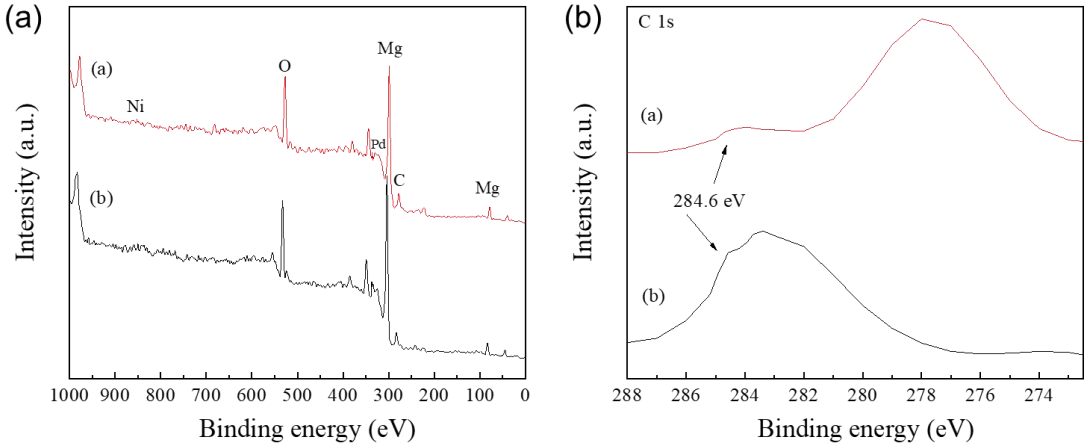

Figure S5 XPS survey spectra (a) and high-resolution C 1s spectra (b) of Mg-PdNi@rGN composite.

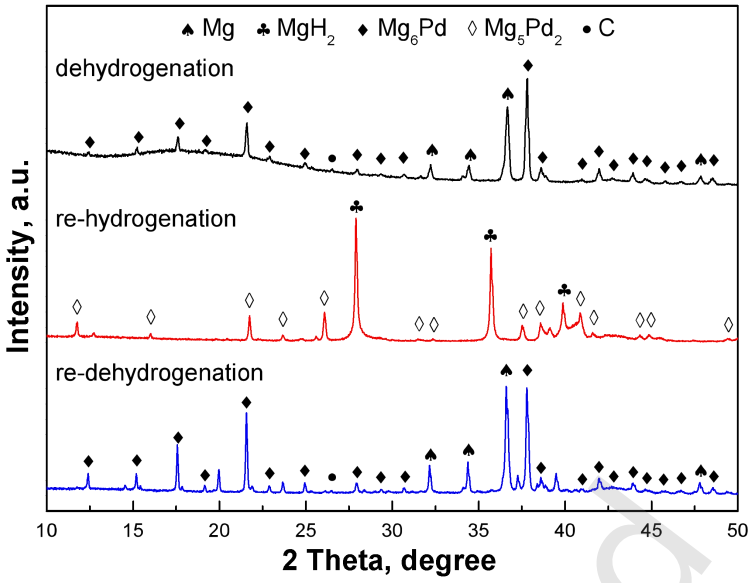

Figure S6 XRD patterns of the MgH2-20wt%Pd composite after dehydrogenation, re-hydrogenation and re-dehydrogenation.